geosciences

MDPI

Article

Ductile Shearing and Focussed Rejuvenation: Records of High-*P* (eo-)Alpine Metamorphism in the Variscan Lower Crust (Serre Massif, Calabria—Southern Italy)

Vincenzo Festa [1], Annamaria Fornelli [1], Francesca Micheletti [1], Richard Spiess [2] and Fabrizio Tursi [1,*]

[1] Department of Earth and Geo-Environmental Sciences, University of Bari Aldo Moro, Via E. Orabona 4, 70125 Bari, Italy; vincenzo.festa@uniba.it (V.F.); annamaria.fornelli@uniba.it (A.F.); francesca.micheletti@uniba.it (F.M.)

[2] Department of Geoscience, University of Padua, Via G. Gradenigo 6, 35131 Padova, Italy; richard.spiess@unipd.it

* Correspondence: fabrizio.tursi@uniba.it or fabrizio.tursi1@gmail.com

Abstract: In the present study, we unveil the real significance of mylonitic reworking of the polymetamorphic crystalline basement in the Serre Massif of Calabria (Southern Italy). We use a multidisciplinary approach to comprehend the structural, microstructural and petrologic changes that occurred along a, so far, not much considered shear zone affecting the Variscan lower crustal rocks. It was never before studied in detail, although some late Cretaceous ages were reported for these mylonites, suggesting that this shear zone is of prime importance. Our observations reveal now that the formation of the new structural fabric within the shear zone was accompanied by changes in mineral assemblages, in a dominant compressive tectonic regime. During this tectono-metamorphic event, high-*P* mylonitic mineral assemblages were stabilized, consisting of chloritoid, kyanite, staurolite, garnet and paragonite, whereas plagioclase became unstable. Average peak *P*–*T* conditions of 1.26–1.1 GPa and 572–626 °C were obtained using THERMOCALC software. These data question (i) that the Serre Massif represents an undisturbed continuous section of the Variscan crust, as generally suggested in the literature, and (ii) highlight the role of (eo-)Alpine high-*P* tectonics in the Serre Massif, recorded within mylonite zones, where the Variscan basement was completely rejuvenated.

Keywords: ductile shear zone; rejuvenation of crystalline basements; eo-Alpine tectonics; HP metamorphism; Calabria polymetamorphic terrane

Citation: Festa, V.; Fornelli, A.; Micheletti, F.; Spiess, R.; Tursi, F. Ductile Shearing and Focussed Rejuvenation: Records of High-*P* (eo-)Alpine Metamorphism in the Variscan Lower Crust (Serre Massif, Calabria—Southern Italy). *Geosciences* **2022**, *12*, 212. https://doi.org/10.3390/geosciences12050212

Academic Editors: Martina Kirilova, Ben Clennell and Jesus Martinez-Frias

Received: 12 April 2022
Accepted: 11 May 2022
Published: 17 May 2022

1. Introduction

In polymetamorphic terranes, ductile shear zones play a pivotal role in the rejuvenation of old continental crust, i.e., new structural fabric formation, overprinting of metamorphic assemblages and ages. They represent the primary loci where metamorphism is readjusted and ductility is enhanced [1]. Their investigation and the unveiling of variations in mineral assemblages within are consequently relevant to understanding the polymetamorphic evolution of old terranes during subsequent orogenic processes. In this manuscript, we focus on a shear zone exposed in the northern Serre Massif (Calabria, Southern Italy) (Figure 1a,b) along which the granulite-pyriclasite and the metapelite units of the lower Variscan crust have been tectonically juxtaposed (Figure 1c). However, this shear zone has so far been neglected in its importance for tectono-metamorphic large-scale reconstructions. In the literature, this shear zone is locally marked by the presence of mylonites [2] ("m" in Figure 1c) or brittle faults [3,4] ("tc" and "f" in Figure 1c) and can be traced for tens of kilometres south of the Curinga–Girifalco Line (CGL) (Figure 1c).

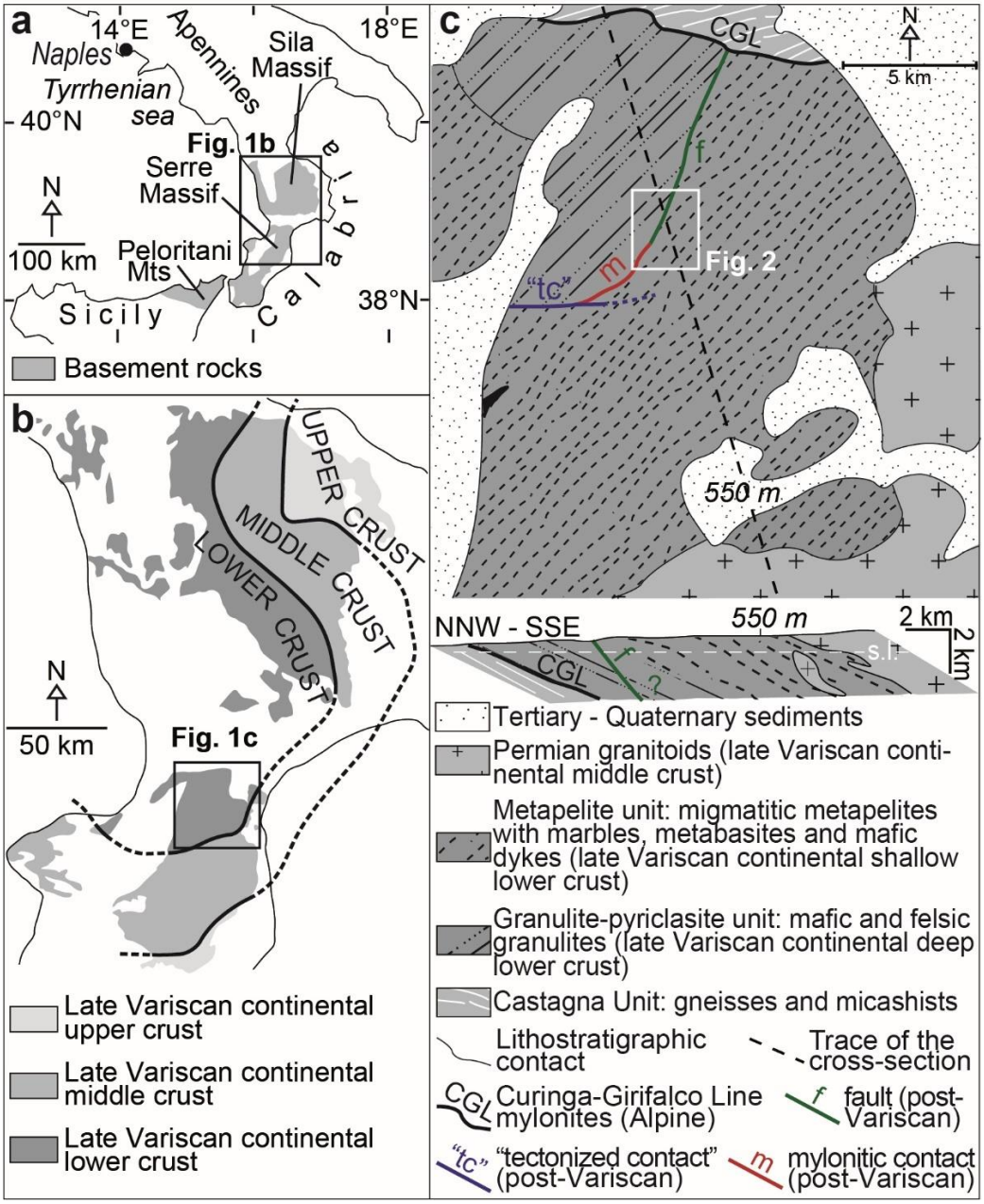

Figure 1. (**a**) Sketch map showing the distribution of basement rocks exposed in Southern Italy (after [5], modified). (**b**) Sketch map of the lower, middle, and upper late-Variscan continental crust exposed in Calabria (after [6], modified). (**c**) Geological sketch map of the northern Serre Massif and regional cross-section (after [7], modified): the traces of the post-Variscan "tectonized contact" ("tc"), mylonitic contact (m) and fault (f) are shown.

It is noteworthy that the Rb-Sr biotite ages of ca. 88 Ma obtained on mylonites of this shear zone led to the hypothesis [8] that crustal tectonic shortening, related to the closure of Tethys ocean, possibly occurred. On this basis, we investigate structurally and petrologically this tectonic contact between the granulite-pyriclasite and the metapelite units in its southern portion, where [2] reported mylonites (Figure 1c). The results of this study open a completely new perspective on the, so far, not considered undisturbed upward stratigraphic continuity of the Variscan lower crust in the Serre Massif. Furthermore, this study highlights the importance of a thorough petrologic investigation to unveil the real significance of mylonitic reworking of polymetamorphic crystalline basements.

2. Geological Setting

The Calabria–Peloritani terrane (Figure 1a) is a nappe stack which includes tectono-metamorphic units of oceanic and continental crust derivation [9]. The ocean-derived units occupy the intermediate portion of the tectonic pile and are mainly represented by ophiolites affected by high-pressure (*HP*)-low-temperature (*LT*) metamorphism, with peak *P*–*T* conditions up to 2.0–2.1 GPa and 475–490 °C [10–16], at ca. 47 Ma [17] and ca. 35 Ma [18].

Continental units belong to the Variscan crystalline basement, and were locally overprinted by Alpine metamorphism up to 0.9–1.0 GPa and 560–590 °C [19–24], rarely reaching the conditions of the amphibolite-eclogite facies transition [25]. According to [26], the metamorphic overprint of the continental crust derived units occurred between 45 Ma and 33 Ma.

In the Serre Massif (Figure 1a), a Variscan continental crustal block, ca. 27 km thick, has been exposed [27] (Figure 1b), from the late Oligocene to present day tilting [28]. It consists, from NW to SE (Figure 1b) and from the bottom to the top, of high- to medium-grade metamorphic rocks (lower crust), granitoids (intermediate crust) and medium- to low -grade phyllites and paragneisses (upper crust) [29]. High-grade metamorphic rocks, greatly characterizing the lower crust (ca. 7–8 km thick), are mainly (i) metagabbros, felsic and mafic granulites (below) and (ii) migmatitic metapelites, with interleaved metabasites and metagreywakes (above) [3,30], which, according to [2,4] form the granulite-pyriclasite (ca. 3 km thick) and the metapelite (ca. 4 km thick) units, respectively (Figure 1c). During meso-Alpine, the Variscan lower crust units overthrusted the Castagna Unit, which was formerly part of the Variscan intermediate crust [31–34], along the Curinga–Girifalco Line (CGL) [20,24,35].

3. Materials and Methods

To reach the objective of the present study, geological mapping at a scale 1: 10,000 was carried out, including both mylonites [2] and brittle faults [4], in the Serre dei Meriani–Passo Fosso del Lupo area, between the granulite-pyriclasite and the metapelite units (Figure 2). During geological mapping, structural data were collected and processed with Stereonet3D software [36]. Kinematic observations on mylonites were made both at outcrop and sample scales, i.e., on oriented rock slabs cut parallel to the X and Z axes of the finite strain ellipsoid, obtained by trace lineation and its normal toward the top, respectively. For the foliation and lineation terminology used in the present article, we refer to [37].

A high-angle transect across the strike of the contact was chosen for sampling mylonites, and twenty samples were collected (Figure 2). Six representative samples showing different degrees of deformation and recrystallization were studied to determine the mineral assemblage variations between mylonites and their Variscan protoliths. Samples were investigated through an EVO-50XVP scanning electron microscope (SEM) of LEO at the Department of Earth and Geo-environmental Sciences, University of Bari Aldo Moro, coupled with an energy-dispersive (ED) Silicon drift Oxford detector (Oxford Instruments) equipped with a Super Atmosphere Thin Window ©. Microanalysis was performed using the ED detector on polished carbon coated thin sections. Operating conditions for quantitative microanalysis were 15 kV accelerating potential, 500 pA probe current, counting time of 50 s and working distance of 8.5 mm.

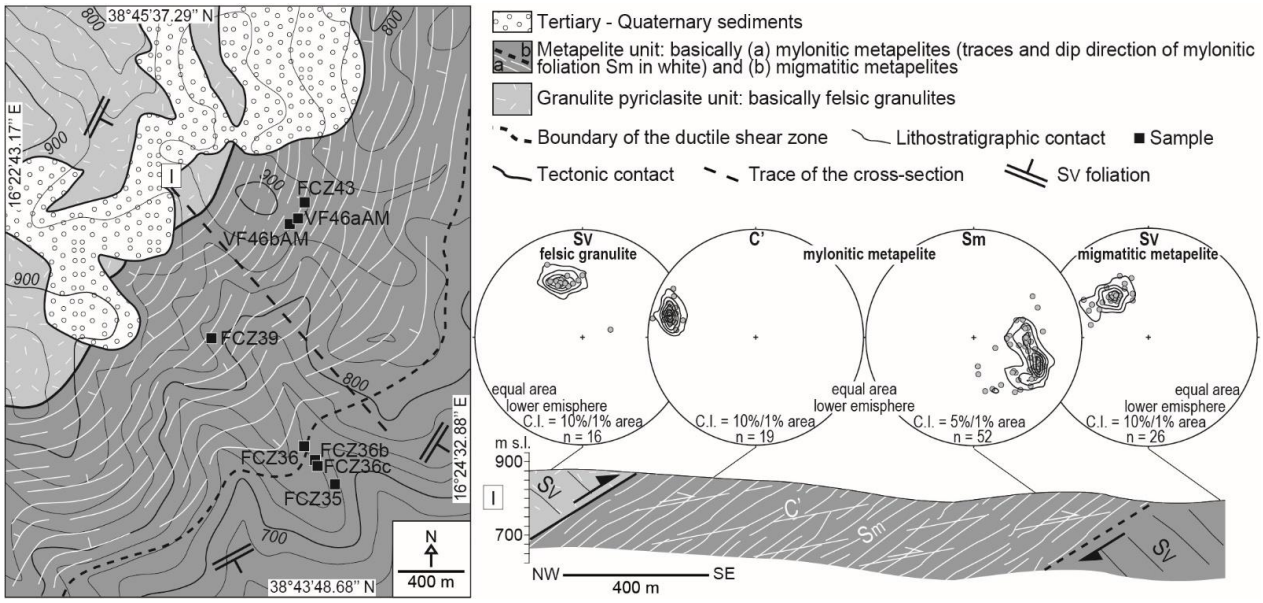

Figure 2. Structural sketch map of the Serre dei Meriani–Passo Fosso del Lupo area (see Figure 1 for location) and geological cross section with stereographic projections (poles) of the S_V and S_m and C′ mylonitic foliations, on top.

4. Results

4.1. Structural Outline

In the Serre dei Meriani–Passo Fosso del Lupo area (Figure 2), the metapelite unit is basically characterized by migmatitic metapelites with interleaved metabasites cropping out to the southeast (Figure 2). It is tectonically juxtaposed to the granulite-pyriclasite unit. The latter unit, typically represented by felsic granulites (Figure 2), crops out in the north-western sector of the area (Figure 2). The lithotypes composing both units show an older Variscan main foliation, hereafter named S_V, particularly evident in the migmatitic metapelites, where it basically consists of an alternation of mm- to cm-thick melanocratic and leucocratic layers (Figure 3a,b). Generally, this foliation moderately dips southeastward (Figure 2). The lithotypes of both units rarely show a well-defined Variscan lineation. When visible, especially in migmatitic metapelites, lineation is defined by the alignment of sillimanite prisms or it is due to the preferred shape orientation of biotite flakes.

The contact between the two units is clearly tectonic, because it is characterized by the presence of mylonites, which formed primarily at the expense of the migmatitic metapelites (Figure 3c–f). Next to the shear zone border, i.e., in the low-strain zones, the migmatitic metapelites locally show generally open folds of the older S_V, related to the mylonitic event (Figure 3b).

The tectonic reworking of the migmatitic metapelites is characterized by a main mylonitic foliation, hereafter S_m (Figure 3c–f), that transects the S_V, as shown at map scale. The S_m foliation is defined by the alternation of fine-grained mica-rich layers and coarser-grained, millimetres- to centimetres-thick, leucocratic layers/lenses (Figure 3e,f), formed by transposition. Millimetre-sized porphyroclasts of comminuted garnets are evident in the mica-rich layers (Figure 3e). Furthermore, extremely fractured garnets form centimetre-sized lens-shaped aggregates (Figure 3e,f), embedded in dynamically recrystallized leucocratic thin layers (Figure 3f), which are detailed in the subsequent section. It is precisely the elongation of the felsic and garnet lenses that can be associated with an aggregate lineation coeval with S_m. Generally, the S_m foliation dips moderately northwestward; this is also the overall dip of the shear zone juxtaposing the granulite-pyriclasite unit, above, and the metapelite unit, below (Figure 2). In the investigated area,

the shear zone has a maximum thickness of ca. 800 m (Figure 2). C′-type shear bands, crosscutting the S_m (Figure 3c–f), and gently dipping west–northwest (Figure 3c,d), give way to C-C′ (where C = S_m) type structures, which overall indicate a top-to-the-SE tectonic transport in the present geographic coordinates, along the shear zone (Figures 2 and 3c–f).

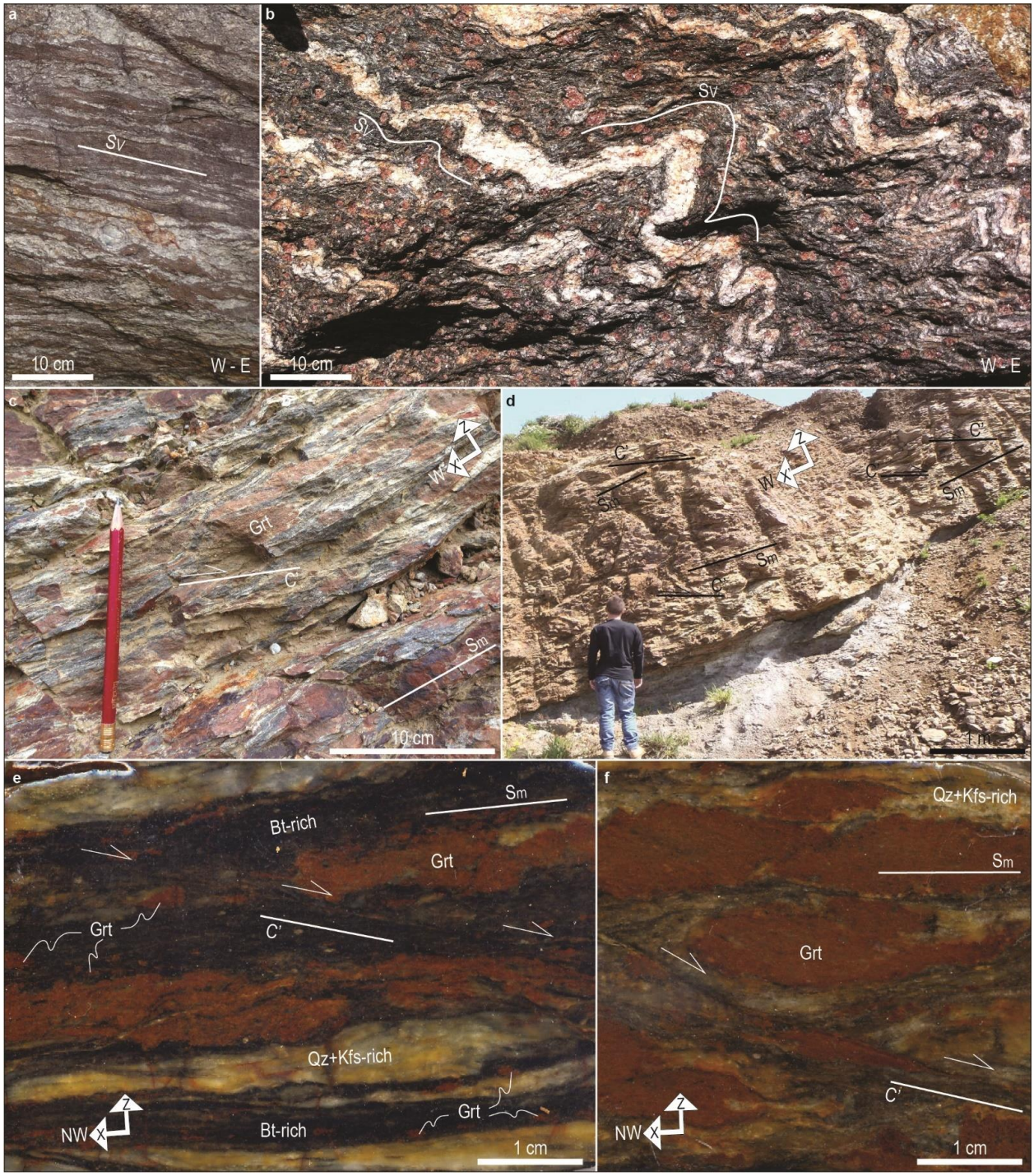

Figure 3. (**a**,**b**) Field examples of layering in migmatitic metapelite; note the evident folding of the layering. (**c**,**d**) Field examples of mylonitic metapelite cropping out in the Passo Fosso del Lupo–Serre dei Meriani area. (**e**,**f**) Polished rock slabs of mylonitic metapelite (sample VF46aAM and VF46bAM, respectively; see Figure 2 for location). S_V = Variscan main foliation, S_m = main mylonitic foliation, C′ = shear bands, Grt = garnet, Bt = biotite, Qz = quartz, Fsp = feldspars, X and Z = maximum and minimum strain axes, respectively, X′ = nearly X-axis. Mineral abbreviations after [38].

4.2. Petrography and Mineral Chemistry

The mineral assemblages of migmatitic metapelites and interleaved metabasites, as well as the related mylonites, are detailed below and summarized in Table 1. Migmatitic metapelites are Grt-Sil paragneisses, whereas the derived mylonites are Grt-Ctd schists (Figure 4). The interleaved mafic rocks consist of Cpx-Opx mafic granulites and mylonitic amphibolites (Figure 5), respectively (mineral abbreviations after [38]).

Table 1. Mineral paragenesis developed during pre-mylonitic and mylonitic events in metapelite and metabasite samples.

Metapelites																		
Sample	**Pre-Mylonitic Assemblage**							**Mylonitic Assemblage**										
	Grt_1	**Sil**	**Bt**	**Pl**	**Rt**	**Kfs**	**Qz**	**Grt_{new}**	**Chl**	**Pg**	**Ctd**	**Ms**	**Mrg**	**Czo**	**Ky**	**St**	**Qz_r**	**Ilm**
FCZ43	core				x			x	x	x	x	x			x	x	x	x
FCZ39	x	x			x		x	x	x	x	x	x	x	x	?		x	x
FCZ 35	x	x	x	x	x	x	x		x			x					x	x
Metabasites																		
Sample	**Pre-Mylonitic Assemblage**							**Mylonitic Assemblage**										
	Cpx	**Opx**	**$Pl_{An50–70}$**	**Parg-Hbl**	**Bt**	**Qz**	**Ilm**	**Act**	**Ms**	**Chl**	**Czo**	**$Pl_{An11–18}$**	**Ilm**	**Qz_r**				
FCZ 36			x	x				x	x	x	x	x	x	x				
FCZ36b	x	x	x	x	x	x	x	x						x				
FCZ36c	x	x	x	x	x	x	x											

? = no clear evidence, r = recrystallised.

The migmatitic Grt-Sil paragneiss (e.g., sample FCZ35) shows a pervasive S_V foliation defined by biotite- and sillimanite-rich layers that alternate with quartz-feldspathic portions, both enveloping dispersed millimetre to centimetre sized garnet porphyroblasts (Figure 4a,d,e). Aligned biotite flakes have X_{Fe} (i.e., Fe/(Fe + Mg)) around 0.41 and TiO_2 contents of 1.40–1.76 wt.% (Table 2); plagioclase in quartz-feldspathic bands has andesine composition with X_{An} = 36–38 mol% (Table 2). Garnet porphyroblasts show corroded rims with handles and lobes (Figure 4d); they are Alm-rich and Grs-poor (Figure 6a) with composition $Alm_{75–70}Py_{20–24}Grs_{3–4}Sps_2$ mol% (Tables 2 and S1). In quartz-feldspathic bands, quartz shows lobate grain boundaries, pinning microstructures and left-over grains (Figure 4e), indicating grain boundary migration (GBM) recrystallisation of quartz that records temperature significantly higher than 500 °C [39] and which is typically observed at granulite facies metamorphic conditions [37].

The Grt-Ctd mylonitic schist (e.g., samples FCZ39, FCZ43) shows a well-defined S_m mylonitic foliation, characterized by aligned white mica-rich layers alternating to quartz-rich ones, both anastomosing lens-shaped garnet aggregates (Figure 4b,c). Moving from migmatitic Grt-Sil metapelite to Grt-Ctd mylonitic schist, a strong grain size reduction occurs (Figure 4a–c), accompanied by a nearly complete substitution of the mineral assemblage in the mylonites (Table 1). The mylonitic mineral assemblage consists of paragonite, muscovite, chlorite, chloritoid, garnet, ilmenite and kyanite (Figure 4f–m); either margarite and epidote or staurolite (Figure 4i,j) can be present, depending on the bulk composition of the protolith. Toward the tectonic contact with the granulite-pyriclasite unit, very few sillimanite and garnet relicts can be locally observed (Figure 4f–h), thereby they are almost completely replaced by kyanite (Figure 4j,k,m) and small, sub-euhedral garnet grains (Figure 4l), respectively. New garnet grains occur preferentially in white mica-rich bands and consist of many sub-euhedral grains (Figure 4l), which overall simulate the shape of the relict large crystal of garnet (Figure 4g,h). SEM imaging and EDS analyses revealed that these new garnet grains grew on relict crystalline seeds (Figure 4h) in strongly deformed samples. The composition of relict garnet seeds is $Alm_{71–80}Py_{10–14}Grs_{3–4}Sps_2$ mol% (Tables 2 and S1), like that of garnet in migmatitic Grt-

Sil paragneiss (Figure 6a). In contrast, within overgrowing rims or in new sub-euhedral grains (Figure 4h,l), the Grs molecule increases up to 21 mol%, and the overall composition changes to $Alm_{67–79}Py_{9–13}Grs_{7–21}Sps_{1–5}$ mol% (Tables 2 and S1), with few differences depending on the composition of the former Variscan metapelite protolith (Figure 6a).

Table 2. Representative analysis of primary minerals composing Grt-Sil migmatitic paragneiss and Grt-Ctd mylonitic schists; "bdl" is an abbreviation for "below detection limit".

	FCZ35			FCZ39									FCZ43					
	Grt	Bt	Pl	Larger Grt		Small Grt		Mrg	Pg	Ms	Ctd	Ep	Small Grt		Pg	Ms	St	Ctd
				Core	Rim 1	Core	Rim						Core	Rim				
SiO_2	38.05	36.88	59.66	38.32	37.85	37.58	37.98	30.73	45.95	47.13	25.34	39.32	37.50	37.69	46.43	46.65	28.33	25.19
TiO_2	bdl	1.40	dbl	bdl	bdl	bdl	bdl	bdl	bdl	bdl	bdl	bdl	bdl	bdl	bdl	0.25	0.35	bdl
Al_2O_3	21.25	18.83	25.75	21.48	21.02	20.84	21.15	50.33	39.96	36.63	41.30	30.54	21.00	20.85	39.87	33.94	53.01	41.26
FeOt	32.42	14.97	bdl	28.71	31.57	35.81	30.15	0.55	0.25	0.65	21.47	3.81	34.19	33.01	0.42	1.25	12.06	21.17
MnO	1.04	bdl	bdl	0.68	1.55	2.08	0.98	bdl	bdl	bdl	bdl	bdl	0.91	0.54	bdl	bdl	bdl	bdl
MgO	5.76	12.23	bdl	8.25	2.42	2.68	2.25	0.30	0.12	0.56	4.32	bdl	3.25	3.03	bdl	1.19	2.05	4.60
ZnO	bdl	bdl	bdl	bdl	bdl	bdl	bdl	bdl	bdl	bdl	bdl	bdl	bdl	bdl	bdl	bdl	1.85	bdl
BaO	bdl	bdl	bdl	bdl	bdl	bdl	bdl	bdl	bdl	bdl	bdl	bdl	bdl	bdl	bdl	0.38	bdl	bdl
CaO	1.36	0.14	7.95	1.46	5.94	1.47	7.76	12.23	1.14	bdl	bdl	24.88	3.00	4.85	0.96	bdl	bdl	bdl
Na_2O	bdl	0.33	7.07	bdl	bdl	bdl	bdl	1.22	5.40	1.34	bdl	bdl	bdl	bdl	5.51	1.08	0.21	bdl
K_2O	bdl	9.36	0.10	bdl	bdl	bdl	bdl	bdl	1.93	9.03	bdl	bdl	bdl	bdl	2.08	9.24	bdl	bdl
Total	99.88	94.14	100.53	98.90	100.35	100.46	100.27	95.36	94.75	95.34	92.43	98.55	99.85	99.97	95.27	93.98	97.87	92.22
O	12.00	11.00	8.00	12.00	12.00	12.00	12.00	11.00	11.00	11.00	12.00	12.50	12.00	12.00	11.00	11.00	46.00	12.00
Si	3.01	2.77	2.65	3.00	3.02	3.02	3.02	2.04	2.96	3.10	2.05	3.00	3.01	3.01	2.98	3.14	7.87	2.04
Al^{IV}	–	1.23	1.35	–	–	–	–	1.96	1.04	0.90	2.95	–	–	–	1.02	0.86	0.13	2.96
Al^{VI}	1.98	0.44	-	1.98	1.97	1.99	1.97	1.98	2.00	1.93	1.00	2.74	1.99	1.97	2.00	1.83	17.22	0.99
Al_{tot}	1.98	1.67	1.35	1.98	1.97	1.99	1.97	3.94	3.04	2.84	3.94	2.74	1.99	1.97	3.02	2.69	17.35	3.95
Ti	–	0.08	–	–	–	–	–	–	–	–	–	–	–	–	–	0.01	0.07	–
Fe^{3+}	0.02	–	–	0.02	0.03	0.01	0.03	–	–	–	–	0.24	0.01	0.03	–	–	0.21	–
Fe^{2+}	2.13	0.94	–	1.87	2.08	2.38	1.98	0.03	0.01	0.04	1.45	–	2.28	2.17	0.02	0.07	2.59	1.44
Mg	0.68	1.37	–	0.96	0.29	0.32	0.27	0.03	0.01	0.05	0.52	–	0.39	0.36	–	–	0.85	0.56
Mn	0.07	–	–	0.05	0.10	0.14	0.07	–	–	–	–	–	0.06	0.04	-	0.12	–	–
Zn	–	–	–	–	–	–	–	–	–	–	–	–	–	–	–	–	0.38	–
Ba	–	–	–	–	–	–	–	–	–	–	–	–	–	–	–	0.01	–	–
Ca	0.12	0.01	0.38	0.12	0.51	0.13	0.66	0.87	0.08	–	–	2.03	0.26	0.42	0.07	–	–	–
Na	–	0.05	0.61	0.02	–	–	–	0.16	0.68	0.17	–	–	–	–	0.69	0.14	0.11	–
K	–	0.90	0.01	–	–	–	–	–	0.16	0.76	–	–	–	–	0.17	0.79	–	–
$\Sigma_{cat.}$	8.01	7.79	4.99	8.02	8.00	8.00	7.99	7.07	6.94	6.95	7.97	8.01	8.00	7.99	6.94	6.97	29.44	7.98
X_{Fe}	0.76	0.41		0.66	0.88	0.88	0.88	0.51	0.54	0.39	0.74		0.85	0.86	1.00	0.37	0.75	0.72
X_{Alm}	0.71			0.62	0.70	0.80	0.67						0.76	0.73				
X_{Prp}	0.23			0.32	0.10	0.11	0.09						0.13	0.12				
X_{Grs}	0.04			0.04	0.17	0.04	0.22						0.09	0.14				
X_{Sps}	0.02			0.02	0.04	0.05	0.02						0.02	0.01				
X_{Adr}	0.01			0.01	0.01	0.00	0.02						0.01	0.02				
X_{An}			0.38															

The new mineral assemblage is dominated by muscovite with Si_{apfu} of 3.10–3.14, Na/(Na + Ca + K + Ba) = 0.15–0.22 (Figure 6b) and X_{Fe} values between 0.37 and 0.51 (Table 2), and by paragonite and margarite with Na/(Na + Ca + K + Ba) of 0.70–0.79 and 0.15 (Figure 6b), respectively, with X_{Fe} values of paragonite that change markedly from ~0.54 to ~1.00 in most deformed samples (Table 2). It is noteworthy that the mylonitic

mineral assemblage is devoid of plagioclase, the latter being the mineral that primarily hosts Na and Ca in migmatitic metapelites; therefore, the formation of paragonite and margarite during the mylonitic event can be closely related to equilibria that destabilised the relict plagioclase. Clinozoisite and chloritoid are new syn-kinematic minerals (Figure 4i–k); the second shows a homogeneous composition (X_{Fe} values of ~0.72); chlorite with X_{Fe} values of 0.32–0.38 is a syn-kinematic mineral too, along with tiny anhedral staurolite intergrown with chloritoid and kyanite (Figure 4j), having X_{Fe} around 0.76, Zn_{apfu} = 0.36–0.41 and Na_{apfu} in X site of ~0.1 (Table 2).

In quartz-rich bands, larger relict quartz crystals show subgrain rotation (SGR) recrystallisation microstructures (Figure 4g) that almost completely replace the older crystals (Figure 4k,m).

The metabasites interleaved with migmatitic metapelites are represented by Cpx-Opx and Amph-bearing mafic granulites (Table 1; Figure 5a–e). These mafic granulites (e.g., sample FCZ36c, FCZ36b) show a slightly developed S_V foliation defined by aligned plagioclase and clinopyroxene, orthopyroxene and amphibole subhedral grains (Figure 5c–e). Clinopyroxene has diopside composition ($Di_{0.60}Hed_{0.30}$) and is in equilibrium with orthopyroxene ($En_{0.47}Fs_{0.52}$), plagioclase (X_{An} = 50–70), biotite (X_{Fe} ~0.50) and ilmenite (Table 3), representing the Variscan granulite facies peak assemblage (Figure 5c). Brown and green amphiboles are related to Variscan post-peak equilibration under amphibolite facies conditions, because it overgrows Cpx, Opx and Bt (Figure 5d,e). As illustrated in Figure 6c, amphibole has primarily pargasite–Fe-pargasite (X_{Fe} = 0.43–0.56) and Mg-hornblende (X_{Fe} = 0.41–0.50) composition (Tables 4 and S2) according to [40]'s nomenclature; in some cases Ca-amphiboles of cummingtonite–grunerite (X_{Fe} = 0.31–0.33) and anthophyllite (X_{Fe} = 0.37–0.39) composition (Tables 4 and S2) show rim overgrowths or intergrowths with Cpx. Rare anhedral quartz grains have curved to straight grain boundaries, indicating that grain boundary area reduction (GBAR) was efficient during post-peak Variscan metamorphism.

Table 3. Representative analysis of pyroxene, mica, plagioclase, chlorite, epidote and ilmenite composing metabasite samples; "bdl" is an abbreviation for "below detection limit".

	FCZ36c					FCZ36b						FCZ36						
	Cpx	Opx	Bt	Pl		Cpx	Opx	Bt	Pl		Ilm	Ep	Chl	Ms	Pl			Ilm
															Relict		New	
				Core	Rim				Core	Rim					Core	Rim		
SiO₂	52.51	51.10	36.74	56.58	54.40	52.65	50.94	36.34	56.82	57.53	0.17	38.35	26.42	45.62	55.29	54.84	65.95	bdl
TiO₂	bdl	bdl	5.66	bdl	bdl	bdl	bdl	4.88	bdl	bdl	54.70	bdl	bdl	bdl	bdl	bdl	bdl	55.58
Al₂O₃	1.08	0.66	14.83	27.45	28.70	0.84	0.50	15.15	27.42	26.31	0.00	28.13	21.51	34.40	28.06	28.04	20.95	bdl
FeOt	11.38	30.68	18.77	bdl	bdl	12.55	32.45	20.12	bdl	bdl	42.93	5.94	20.20	1.11	bdl	bdl	bdl	40.75
MnO	0.32	0.78	bdl	bdl	bdl	0.44	1.33	bdl	bdl	bdl	2.43	0.23	0.26	bdl	bdl	bdl	bdl	2.44
MgO	12.00	15.74	10.68	bdl	bdl	11.15	14.42	9.36	bdl	bdl	bdl	bdl	17.87	0.92	bdl	bdl	bdl	0.14
BaO	bdl	bdl	bdl	bdl	bdl	bdl	bdl	bdl	bdl	bdl	bdl	bdl	bdl	0.66	bdl	bdl	bdl	bdl
CaO	22.91	0.46	-bdl	10.10	11.89	22.74	0.45	0.17	9.87	9.03	bdl	23.63	0.24	0.15	10.89	10.92	2.22	bdl
Na₂O	0.26	bdl	bdl	5.68	4.84	0.23	bdl	0.11	6.02	6.43	bdl	bdl	bdl	1.08	5.44	5.40	9.80	bdl
K₂O	bdl	bdl	9.98	0.19	0.11	bdl	bdl	9.58	0.22	0.19	bdl	bdl	bdl	9.96	bdl	bdl	bdl	bdl
Total	100.46	99.42	96.66	100.00	99.94	100.60	100.09	95.71	100.35	99.49	100.23	96.28	86.50	93.90	99.68	99.20	98.92	98.91
O	6.00	6.00	11.00	8.00	8.00	6.00	6.00	11.00	8.00	8.00	3.00	12.50	14.00	11.00	8.00	8.00	8.00	3.00
Si	1.97	2.00	2.76	2.54	2.46	1.99	2.00	2.78	2.54	2.59	–	3.01	2.74	3.09	2.50	2.49	2.92	–
Al^{IV}	0.03	–	1.24	1.45	1.53	0.01	–	1.22	1.45	1.40	–	–	1.26	0.91	1.49	1.50	1.09	–
Al^{VI}	0.02	0.03	0.08	–	–	0.03	0.02	0.14	–	–	–	2.60	1.37	1.84	–	–	–	–
Al_{tot}	0.05	0.03	1.32	1.45	1.53	0.04	0.02	1.36	1.45	1.40	–	2.60	2.63	2.75	1.49	1.50	1.09	–
Ti	–	–	0.32	–	–	–	–	0.28	–	–	1.02	–	–	–	–	–	–	1.05
Fe^{3+}	0.03	–	-	–	–	–	–	–	–	–	–	0.38	–	–	–	–	–	–

Table 3. *Cont.*

	FCZ36c					FCZ36b						FCZ36						
	Cpx	Opx	Bt	Pl		Cpx	Opx	Bt	Pl		Ilm	Ep	Chl	Ms	Pl			Ilm
															Relict		New	
				Core	Rim				Core	Rim					Core	Rim		
Fe^{2+}	0.33	1.01	1.18	–	–	0.39	1.07	1.29	–	–	0.89	0.01	1.75	0.06	–	–	–	0.85
Mg	0.67	0.92	1.20	–	–	0.63	0.85	1.07	–	–	-	-	2.77	0.09	–	–	–	0.01
Mn	0.01	0.03	–	–	–	0.01	0.04	–	–	–	0.05	0.02	0.02	–	–	–	–	0.05
Ba	–	–	–	–	–	–	–	–	–	–	–	–	–	0.02	–	–	–	–
Ca	0.92	0.02	–	0.49	0.58	0.92	0.02	0.01	0.47	0.44	–	1.99	0.03	0.01	0.53	0.53	0.11	–
–Na	0.02	–	–	0.50	0.42	0.02	–	0.02	0.52	0.56	–	–	–	0.14	0.48	0.48	0.84	–
K	–	–	0.96	0.01	0.01	–	–	0.93	0.01	0.01	–	–	–	0.86	–	–	–	–
$\Sigma_{cat.}$	4.00	4.00	7.74	4.98	4.99	4.00	4.00	7.74	5.00	5.00	1.97	8.00	9.94	7.02	4.99	5.00	4.96	1.95
X_{Fe}	0.33	0.52	0.50			0.38	0.55	0.55			0.95		0.39	0.40				0.94
X_{An}				0.49	0.57				0.47	0.43					0.53	0.53	0.11	

Table 4. Representative analysis of amphiboles in metabasite samples; "bdl" is an abbreviation for "below detection limit".

	FCZ36c	FCZ36b				FCZ36				
						Relict Porphyroclast			Syn-Kinematic	
	Mg-Hbl	Parg	Mg-Hbl	Gru	Ath	Parg	Mg-Hbl	Fe-Hbl	Act	
		Core	Rim	Hbl_r	Cpx_r	Core	Rim	Deformation Tail	Core	Rim
SiO_2	44.46	43.80	51.09	52.85	51.27	44.24	43.03	42.77	54.02	55.34
TiO_2	1.45	1.88	0.25	bdl	0.22	1.47	0.33	0.36	bdl	bdl
Al_2O_3	10.89	10.80	5.39	0.76	2.46	11.07	15.61	16.57	1.42	1.40
FeOt	16.14	18.11	15.16	26.31	25.47	15.83	15.68	15.93	15.02	11.66
MnO	0.00	0.27	0.22	0.69	0.58	0.23	0.25	0.26	0.32	0.24
MgO	10.10	9.03	13.41	14.57	12.84	9.73	8.43	7.83	14.24	16.90
CaO	12.03	11.82	11.84	0.92	3.06	11.64	11.45	11.32	12.34	12.25
Na_2O	0.95	1.29	0.49	bdl	0.18	1.44	1.81	1.88	0.17	0.15
K_2O	1.24	1.25	0.38	bdl	0.09	0.91	0.57	0.50	bdl	bdl
Total	97.26	98.25	98.23	96.10	96.17	96.56	97.16	97.42	97.53	97.94
O	22.00	22.00	22.00	22.00	22.00	22.00	22.00	22.00	22.00	22.00
Si	6.66	6.58	7.39	7.98	7.78	6.70	6.41	6.35	7.85	7.87
Al^{IV}	1.34	1.42	0.61	0.02	0.22	1.30	1.59	1.65	0.15	0.13
Al^{VI}	0.59	0.50	0.31	0.12	0.22	0.67	1.15	1.25	0.10	0.11
Al_{tot}	1.92	1.91	0.92	0.14	0.44	1.98	2.74	2.90	0.24	0.24
–Ti	0.16	0.21	0.03	-	0.03	0.17	0.04	0.04	-	-
Fe^{3+}	0.32	0.42	0.22	-	0.02	0.13	0.08	0.07	0.06	0.04
Fe^{2+}	1.70	1.86	1.61	3.32	3.21	1.88	1.88	1.91	1.77	1.35
Mg	2.26	2.02	2.89	3.28	2.91	2.20	1.87	1.73	3.09	3.58
Mn	-	0.03	0.03	0.09	0.08	0.03	0.03	0.03	0.04	0.03
Ca	1.93	1.90	1.84	0.15	0.50	1.89	1.83	1.80	1.92	1.87
Na	0.28	0.38	0.14	-	0.05	0.42	0.52	0.54	0.05	0.04
K	0.24	0.24	0.07	-	0.02	0.18	0.11	0.10	-	-
$\Sigma_{cations}$	15.47	15.56	15.14	14.95	15.03	15.55	15.50	15.48	15.02	15.01
X_{Fe}	0.43	0.47	0.36	0.50	0.52	0.46	0.50	0.52	0.36	0.27

r = replacement.

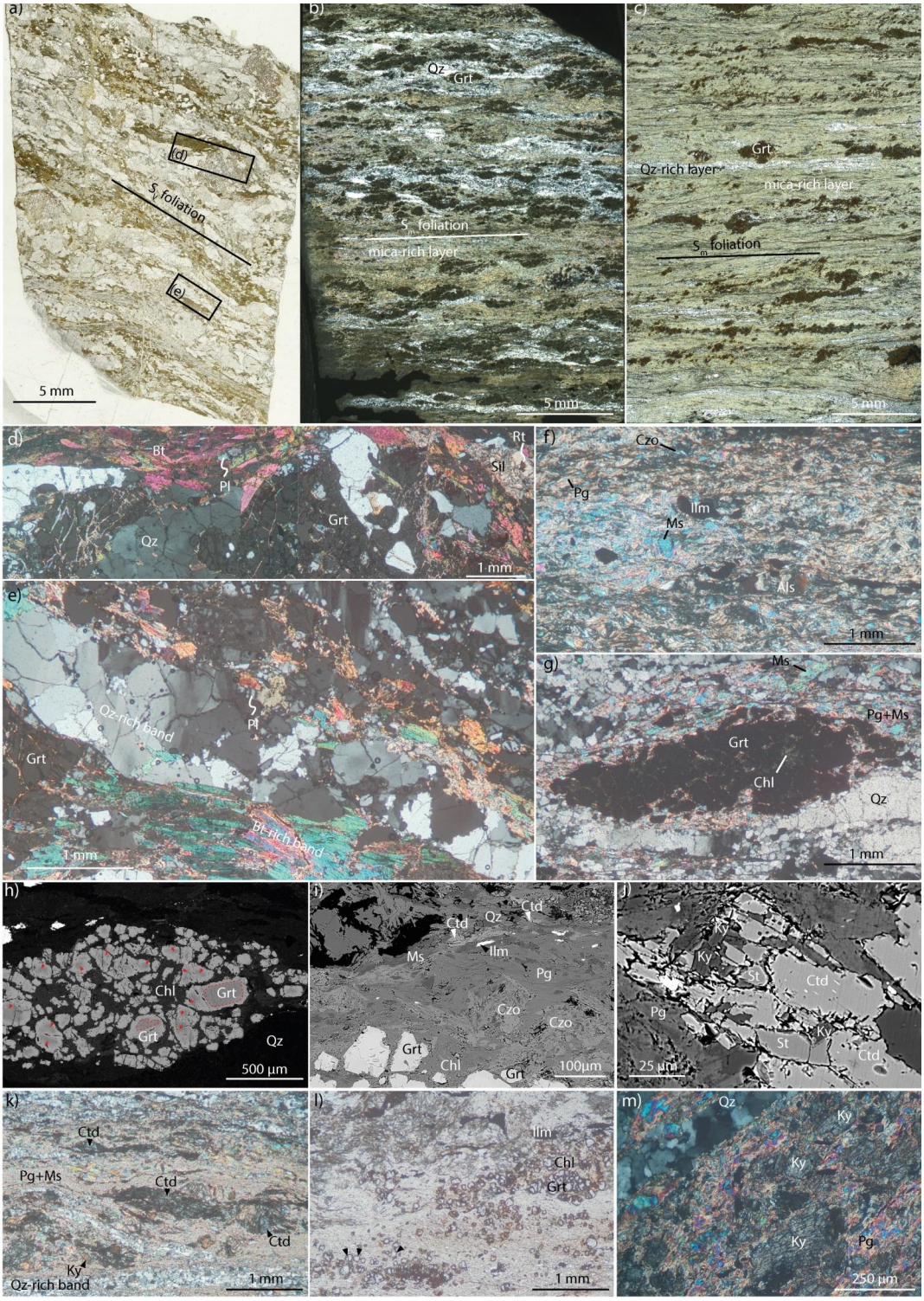

Figure 4. (**a**–**c**) Scanned thin sections of Grt-Sil migmatitic paragneiss (sample FCZ35) and Grt-Ctd mylonitic schists (samples FCZ39, FCZ43) under plane polarized light (**a**), hereafter PPL, and cross-polarized (**b**,**c**) light, hereafter CPL. (**d**) Microphotograph highlighting a Grt porphyroblast in a quartz-feldspathic layer, anastomosed by a Bt-Sil-rich one (sample FCZ35; CPL). (**e**) Quartz-feldspathic layer alternating to a Bt-rich one in sample FCZ35; note pinning microstructures and left-over grains of Qz indicating GBM recrystallisation; CPL microphotograph. (**f**) Detail of a mica-rich layer in sample FCZ39 where Pg and Ms occur together with Als; CPL microphotograph. (**g**) Lens-shaped garnet aggregate between a thin mica-rich band and Qz-rich bands; note SGR recrystallisation of Qz; sample

FCZ39, CPL microphotograph. (**h**) SEM-BSE imaging of the lens-shaped garnet aggregate in (**g**); note darker relict cores and brighter rims of garnet grains related to compositional variations (see text for explanation). (**i**) SEM-BSE imaging highlighting syn-kinematic Ctd and Czo in a mica-rich band; sample FCZ39. (**j**) SEM-BSE imaging of a reaction microdomain where Ctd, St and Ky coexist altogether in a mica-rich band; sample FCZ43. (**k**) Syn-kinematic Ctd and Ky in a Pg-Ms-rich band; note Qz new grains in the Qz-rich band; Sample FCZ43, CPL microphotograph. (**l**) Detail of comminuted garnet in a mica-rich band with chlorite between the small garnet grains; note small sub-euhedral garnet grains (black arrow) in the lower left side; sample FCZ43, PPL microphotograph. (**m**) Aligned syn-kinematic Ky in a Pg-rich band alternating to a thin band of fine-grained recrystallised Qz; sample FCZ43, CPL microphotograph.

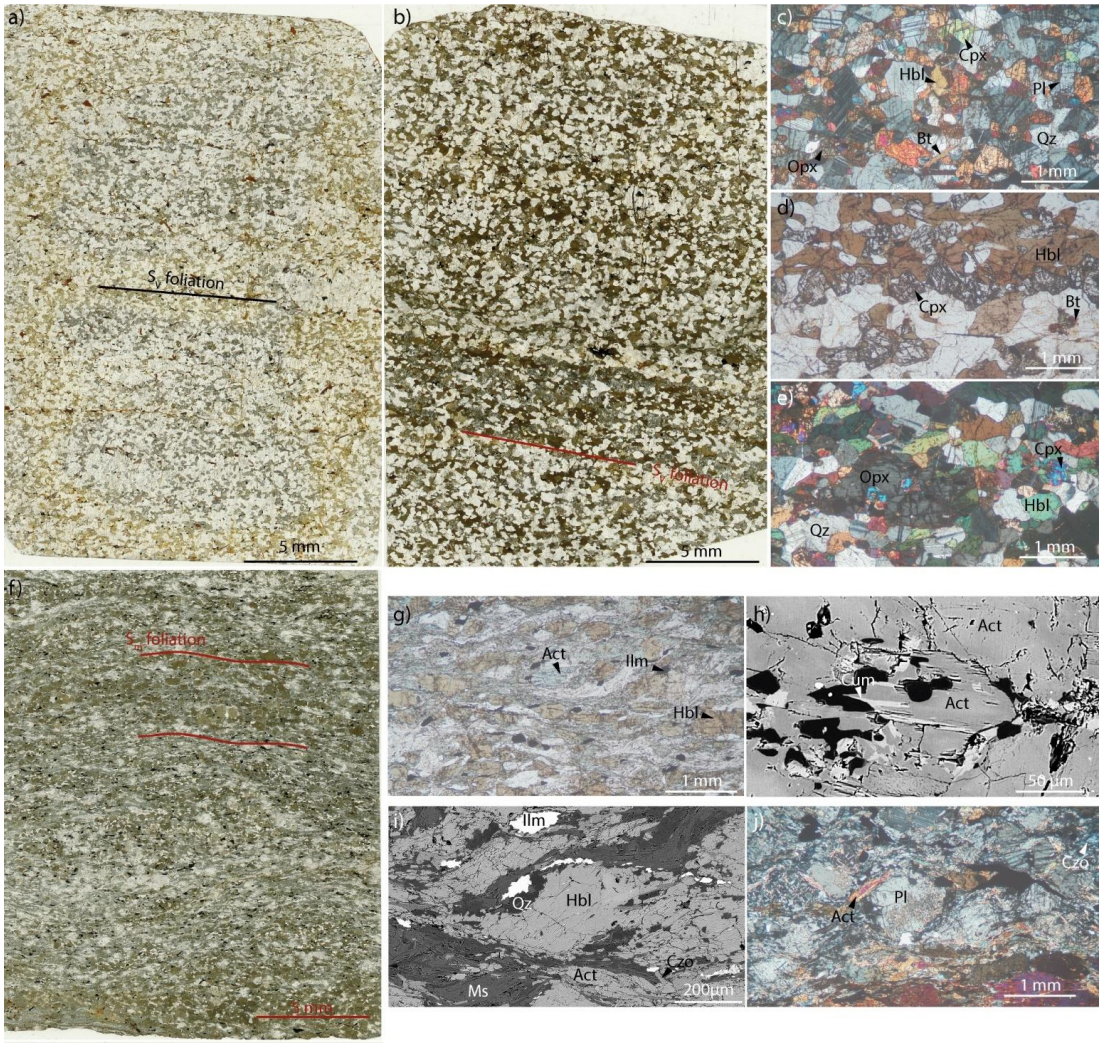

Figure 5. (**a**,**b**) Scanned thin sections under PPL of Cpx-Opx mafic granulite (sample FCZ36c) and Amph-bearing mafic granulite (sample FCZ36b). (**c**) Microphotograph highlighting the Variscan peak metamorphic mineral assemblage (sample FCZ36c; CPL). (**d**,**e**) Detail of aligned Hbl overgrowing Cpx ((**d**); PPL) and Opx ((**e**); CPL) (sample FCZ36b). (**f**) Scanned thin sections under PPL of mylonitic amphibolite (sample FCZ36). (**g**) Detail of pale-green Act anastomosing pre-kinematic Hbl porphyroclasts (sample FCZ36; PPL). (**h**) SEM-BSE imaging showing occasional intergrowths of Act and Cum (sample FCZ36). (**i**) Detail of a Hbl porphyroclast showing handles and lobes at the contact with Qz (sample FCZ36; SEM-BSE imaging; shear sense: top right). (**j**) Microphotograph of sericitized pre-kinematic Pl porphyroclast enveloped by a fine-grained recrystallised quartz-feldspathic matrix (sample FCZ36; CPL).

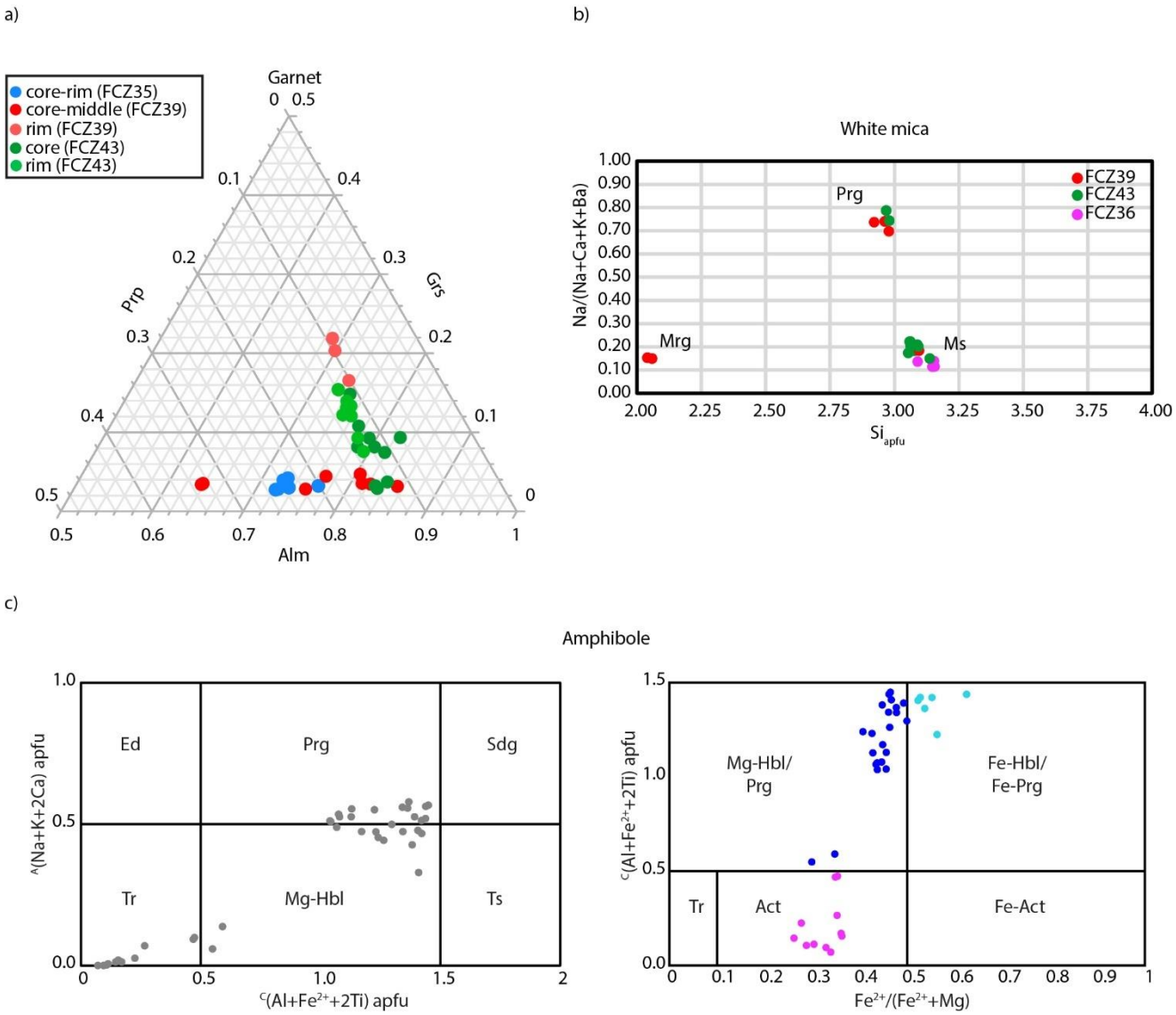

Figure 6. (**a**) Garnet Alm-Prp-Grs compositional triangle; note the overlapping between the composition of garnet porphyroblast in Grt-Sil migmatitic paragneiss (sample FCZ35) and that of the relict cores of garnet in Grt-Ctd mylonitic schists (samples FCZ39, FCZ43). Note how the composition of garnet in Grt-Sil migmatitic paragneiss is homogeneous from core to rim and it is very similar to that of the relict cores and middle in Grt-Ctd mylonitic schists but strongly differs from that in the rim or in the new Grt grains, which are Ca-richer. (**b**) Si_{apfu} vs. Na/(Na + Ca + K + Ba) diagram highlighting the different composition of white micas in mylonitic samples. (**c**) Classification diagrams of Ca-amphiboles in metabasites. Left side: common compositional diagram with boundaries for Ca-amphiboles; projection is on Mg-pure endmembers, according to [40]. Right side: Ca-amphibole compositional diagram constructed by projecting from the A site: the composition of the amphibole in Opx-Cpx and Amph-bearing mafic granulite and the core pre-kinematic amphibole in mylonitic amphibolite is coloured in blue, that of the rim and deformation tail in mylonitic amphibolite is coloured in sky blue and that of the amphibole in the matrix of the mylonitic amphibolite is coloured in magenta.

The Variscan mineral assemblages of Cpx-Opx and Amph-bearing mafic granulites are partially replaced in mylonitic amphibolites (e.g., sample FCZ36; Table 1), which shows a well-developed S_m foliation (Figure 5f), mainly defined by aligned tiny amphibole prisms (Figure 5g). The amphibole defining the mylonitic foliation is a pale green to uncoloured

actinolite (Figure 5g), characterized by X_{Fe} = 0.26–0.35 (Tables 4 and S2), occasionally showing intergrowths (Figure 5h) with cummingtonite (X_{Fe} = 0.38; Tables 4 and S2). Actinolite wraps around pre-kinematic brown and green amphibole porphyroclasts (Figure 5i) of pargasite–Fe-pargasite and Mg-hornblende–Fe-hornblende composition, with Fe-rich compositions especially focussed within porphyroblasts' deformation tail (Figure 6c). The new mylonitic mineral assemblage is also comprised of syn-kinematic clinozoisite, muscovite with Si_{apfu} of ~3.09 and chlorite with X_{Fe} of ~0.40 (Table 3). Fine grained recrystallised quartz and plagioclase of oligoclase composition (X_{An} = 0.11–0.16), in most cases, wrap around pre-kinematic plagioclase porphyroclasts (Figure 5j) of labradorite composition (X_{An} of ~0.53); in addition, ilmenite completes the mineral assemblage (Table 1).

4.3. Thermobarometry

The progressive formation of new minerals from the host rocks toward the core of the shear zone (Table 1) indicates that different equilibration volumes developed in mylonites, in relation to the shearing event. In metapelites, a complete replacement of the protolith's mineral assemblage within the shear zone can be observed in sample FCZ43 (Table 1); whereas, among the investigated metabasites, a broad but uncomplete mineral replacement occurred in sample FCZ36 (Table 1). To constrain the pressure (*P*) and temperature (*T*) conditions at which the mylonitic mineral assemblages equilibrated, optimal thermobarometry was applied to selected samples of Grt-Ctd mylonitic schist (FCZ43) and mylonitic amphibolite (FCZ36). Optimal equilibrium *p*–*T* conditions were obtained through the average *P*–*T* tool (av*PT*) of the software THERMOCALC v3.45 [41,42], with the updated version of the ds62 thermodynamic dataset [43]. The software AX62 (https://filedn.com/lU1GlyFhv3UuXg5E9dbnWFF/TJBHpages/index.html, accessed on 11 April 2022) was employed to obtain activity–composition (*a*–*X*) relationships from the analysed minerals, composing the effective equilibration volume. These *a*–*X* relationships were then used by the av*PT* tool as starting guesses for optimal thermobarometry. In this way, the uncertainties related to thermodynamic interaction energies and end-members composition can be statistically minimized, and the optimal *P*–*T* range, where the calculated independent set of reactions intersects in the *P*–*T* space, can be obtained [44]. For the Grt-Ctd mylonitic schist, the equilibration volume consists of Grt_{new} + Ky + Ctd + Chl + Pg + Qz + Ilm, whereas Act + Ms + Chl + Czo + Pl_{An11} + Qz + Ilm compose the equilibrium mineral assemblage of the mylonitic amphibolite (Table 1). In av*PT* calculations, a fluid of pure H_2O composition was considered, as neither calcite nor graphite were detected; this fluid was set in excess because different OH-bearing minerals developed in the mylonitic mineral assemblages (Table 1). Kyanite and quartz were assumed as pure end members whereas the composition of the other minerals used for av*PT* calculations is reported in Table S3. Staurolite composition for optimal thermobarometry was recalculated devoid of zinc, so that the X_{Fe} remained unchanged, because Zn substitutes for Fe, Mg and Mn indifferently in T2 and M1–M4 sites [45].

A complete independent set of reactions was obtained for both mylonites, with σ_{fit} values below the cut-off (Table 5), indicating that the X^2 test was passed [44]. The mineral assemblage of the Grt-Ctd mylonitic schist (sample FCZ43) records equilibration at 1.26 ± 0.09 GPa and 572 ± 8 °C, with σ_{fit} very close to unity (Table 5). The equilibrium volume in mylonitic amphibolite (sample FCZ36) records equilibration at 1.1 ± 0.16 GPa and 626 ± 61 °C, with σ_{fit} higher than in the Grt-Ctd mylonitic schist but lower than the cut-off value (Table 5). Compared with the av*PT* results, their uncertainties and considering the goodness of each σ_{fit}, the *P*–*T* conditions of equilibration of the Grt-Ctd mylonitic schist fall within the range of those of mylonitic amphibolites. Therefore, the optimal *P*–*T* conditions for equilibration of minerals during the shearing event can be defined in the *P* range of 1.26−1.1 GPa, with temperature varying between 572 and 626 °C.

Table 5. Independent set of reactions calculated with THERMOCALC for a reference *T* and condensed av*PT* results for selected mylonitic samples. Abbreviations after [46].

Grt-Ctd Mylonitic Schist (Sample FCZ43)								
Independent Set of Reactions for *T* = 550°, *X*H_2O = 1.0								
							P(*T*)	sd(*P*)
(1) 17clin + 8mst = 11py + 72mctd + 3ames							11.70	3.12
(2) ames + 2ky = 4mctd							12.00	2.06
(3) py + 5ames + 4q = 8mctd + 3clin							10.60	2.82
(4) 4py + 39mctd = 7clin + 4mst + 3H_2O							11.50	2.70
(5) 17daph + 8fst + 6ky = 11alm + 84fctd							15.00	2.52
(6) 19daph + 10fst + 3q = 13alm + 96fctd							14.90	2.43
(7) 17daph + 6ma + 8fst = 2gr + 9alm + 90fctd							14.20	2.12
(8) 2py + 3ames + 6ma = 2gr + 18mctd							12.00	1.53
Av*PT* for *X*H_2O = 1.0; fit cut-off = 1.45								
	avP	sd	avT	sd	cor	fit		
Lsq	12.60	0.90	572	8	0.018	1.07		
Mylonitic amphibolite (sample FCZ36)								
Independent set of reactions for *T* = 550°, *X*H_2O = 1.0								
							P(*T*)	sd(*P*)
(1) 15ames + 6cz + 5tr + 7q = 17clin + 22an							14.40	1.72
(2) 5ames + 6cz + 5ts + 7q = 7clin + 22an							9.40	3.33
(3) 12cz + 5ts + 14q = 28an + 3tr + 8H_2O							7.70	2.33
(4) 4clin + 6pa = 5ames + 6ab + 2q + 2H_2O							3.60	2.05
(5) clin + fact = daph + tr							13.00	21.97
(6) 15mu + 6cz + 5tr + 7q = 2clin + 22an + 15cel							10.80	1.40
(7) 15mu + 6cz + 5tr + 7q = 2clin + 22an + 15cel							9.70	1.58
(8) 7daph + 25fcel + 12cz + 14q = 25mu + 12fact + 22H_2O							6.10	5.65
(9) 7daph + 25fcel + 12cz + 14q = 25mu + 12fact + 22H_2O							11.00	2.71
(10) daph + 3ab + 2an + q = 3pa + fact							4.40	212.03
(11) 6pa + 5fcel = daph + 6ab + 5mu + 2q + 2H_2O							8.90	42.03
(12) ames + fcel + geik = clin + mu + ilm							8.10	19.05
Av*PT* for *X*H_2O = 1.0; fit cut-off = 1.35								
	av*P*	sd	av*T*	sd	cor	fit		
Lsq	11.00	1.60	626	61	0.933	1.30		

5. Discussion and Conclusions

The results of the present research study are a step forward in the framework of the relationships between ductile shearing and rejuvenation of crystalline basements during tectono-metamorphic events, e.g., [1]. Furthermore, we introduce new data for the evolution of the Variscan continental crust exposed in the Serre Massif, where, until today, HP metamorphic conditions related to post-Variscan tectonics were never documented.

Regarding rejuvenation of the mineral assemblage of Variscan migmatitic metapelites in the Serre dei Meriani–Passo Fosso del Lupo area, the formation of OH-bearing minerals evidences that fluid activity played an important role during post-Variscan mylonitization. Moreover, the growth of kyanite, together with chloritoid, staurolite, paragonite and garnet, as well as the absence of plagioclase, indicate that the shear zone was the primary site where reactions were favoured and HP-metamorphism was recorded. As a matter of fact, whereas mylonites record eclogite facies conditions of 1.26–1.10 GPa and 572–626 °C, the granulites and the migmatitic metapelites out of the shear zone do not show any evidence of post-Variscan equilibration. The mineralogical compatibility between the mylonites and their metapelite protolith indicates that the shear zone was the location of the internally released fluid (e.g., [47]), promoting mineral equilibration under those *P*–*T* conditions. Fluid was reasonably released into the system by biotite breakdown, and, following [48], promoted deformation via reaction-induced rheological weakening, giving rise to a positive feedback effect within the shear zone. A widespread structural reworking occurred especially within

the migmatitic metapelites, which, unlike felsic granulites (Figure 2), contained abundant biotite (e.g., Figures 3a,b and 4a,d,e). In our opinion, the consequence of this feedback effect within the migmatitic metapelites is a progressive increase in thickness of the shear zone, especially in the footwall, up to ca. 800 m (Figure 7). The cartoon of Figure 7 illustrates three time slots with the future shear zone nucleating as reverse fault in a dominant compressive regime (left), that, with time, evolved to a widening ductile shear zone (centre to right). Rejuvenation and equilibration of mineral assemblages is only recorded in the shear zone, where peak-*P* of ~1.2 GPa and T of ~600 °C are registered by the mylonitic rocks. Outside the shear zone, the Variscan *P*–*T* conditions and rock fabric (e.g., Sv foliation) are still preserved. The dominant reverse kinematics during the shear zone evolution is revealed by C-C′ type structures (Figures 2 and 3c–f); in addition, folds of the Variscan foliation affecting migmatitic metapelites in the footwall (e.g., Figure 3b) are evidence of the compressional character of the shear zone. The relatively low-*P* conditions at the end of the Variscan orogeny recorded by the granulite-pyriclasite (~0.70 GPa) and metapelite (~0.50 GPa) units [7,49], as opposed to the high-*P* ones (~1.20 GPa, i.e., ca. 45 km depth) characterising equilibration during the post-Variscan shearing event, indicate that the shear zone developed during crustal thickening and shortening (Figure 7). The relevance of this shear zone, together with the different and diachronic metamorphic Variscan evolution between the granulite-pyriclasite and metapelite units [50], draw into question the upward continuity of the Variscan lower continental crust in the Serre Massif.

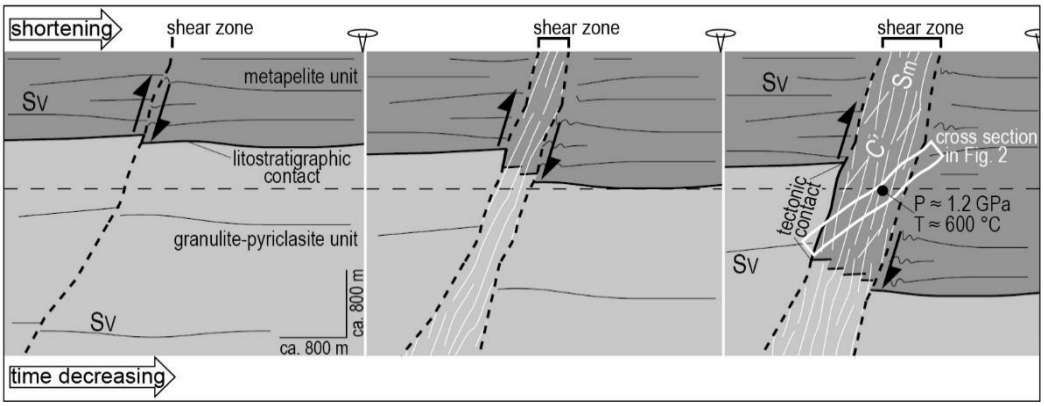

Figure 7. Synoptic sketch showing the evolution of the (eo-)Alpine shear zone of the Serre dei Meriani-Passo Fosso del Lupo area, before the occurrence of crustal tilting that began in the late Oligocene. Note the nucleation of the future shear zone as reverse fault (**left**), ductile widening with time (**centre** to **right**) and *P*–*T* equilibration only in the shear zone (**right**).

It is noteworthy that in the Serre dei Meriani–Passo Fosso del Lupo area (Figure 2), structural and mineral rejuvenation are accompanied by younger ages. Dating of partially equilibrated mylonitic metapelites shows a general rejuvenation of Rb-Sr biotite ages up to 88 Ma, suggesting that the mylonitic event was possibly related to Alpine tectonics [8]. One argument for the Alpine tectono-metamorphic event is that biotite was a relict mineral in the mylonitic metapelite dated by [8], being replaced by white mica during the shearing event. However, considering the thermal sensitivities of the dating systems, i.e., open system behaviour for Rb–Sr in the biotite close to 400 °C [51], the age of the mylonitic event could be in line with eo-Alpine (Upper Cretaceous) tectonics [52,53].

Moreover, a timing constraint can be obtained by the crosscutting relationships between the shear zone and the Alpine CGL, both recording comparable equilibration conditions during shearing [20]. At map scale, the investigated shear zone predates the activity of the CGL, the latter dates back to the Lutetian [54], and transects the tectonic contact between the granulite-pyriclasite and the metapelite units (Figure 1c) [4].

However, because post-Variscan metamorphism and tectonics in the Calabria–Peloritani terrane are framed from Meso-to Neo-alpine [12,15–17,19,21–25] ages, the possible eo-Alpine

tectono-metamorphic event discussed in the present article represents an intriguing aspect that needs to be further constrained.

Supplementary Materials: The following supporting information can be downloaded at: https://www.mdpi.com/article/10.3390/geosciences12050212/s1, Table S1: Analysis of garnet in Grt-Sil migmatitic paragneiss and Grt-Ctd mylonitic schists; "bdl" is an abbreviation for "below detection limit", Table S2: Analysis of amphibole in Cpx-Opx mafic granulite and mylonitic amphibolite; "bdl" is an abbreviation for "below detection limit", Table S3: Analysis of minerals used for av*PT* calculations, recalculated through the software AX62 (see text for details); "bdl" is an abbreviation for "below detection limit".

Author Contributions: Conceptualization, V.F., A.F., R.S., F.T.; methodology, V.F., A.F., F.T.; formal analysis, V.F., F.T.; investigation, V.F., A.F., F.M., R.S., F.T.; data curation, V.F., F.T.; writing—original draft preparation, V.F., A.F., F.T.; writing—review and editing, V.F., A.F., F.M., R.S., F.T.; visualization, V.F., F.T.; supervision, A.F., R.S. All authors have read and agreed to the published version of the manuscript.

Funding: V.F. acknowledges "Fondo per le Attività Base di Ricerca–2017" (UPB FESTA007556FABR). AF is grateful for funds from the University of Bari Aldo Moro; grant n. 00596609 ricat 01. RS acknowledges financial support from PRIN (20178LPCP).

Acknowledgments: We thank two anonymous reviewers for their constructive comments and suggestions. The editorial staff is thanked for carefully handling the manuscript. All authors are grateful to Nicola Mongelli for assistance during the SEM session.

Conflicts of Interest: The authors declare no conflict of interest.

References

1. Holdsworth, R.E.; Hand, M.; Miller, J.A.; Buick, I.S. Continental reactivation and reworking: An introduction. *Geol. Soc. Spec. Publ.* **2001**, *184*, 1–12. [CrossRef]
2. Schenk, V. Petrology of felsic granulites, metapelites, metabasics, ultramafics, and metacarbonates from Southern Calabria (Italy): Prograde metamorphism, uplift and cooling of a former lower crust. *J. Pet.* **1984**, *25*, 255–296. [CrossRef]
3. Piccarreta, G.; Amodio-Morelli, L.; Pagljonico, A. Evoluzione metamorfica delle rocce in facies granulitica nelle Serre nord-occidentali (calabria). *Boll. Della Soc. Geol. Ital.* **1973**, *92*, 861–889.
4. Kruhl, J.H.; Huntemann, T. The structural state of the former lower continental crust in Calabria (S. Italy). *Geol. Rundsch.* **1991**, *80*, 289–302. [CrossRef]
5. Festa, V.; Messina, A.; Paglionico, A.; Piccarreta, G.; Rottura, A. Pre-Triassic history recorded in the Calabria-Peloritani segment of the Alpine chain, southern Italy. An overview. *Period. Mineral.* **2004**, *73*, 57–71.
6. Dubois, R. Définition d'un socle antéhercynien en Calabre. *Comptes Rendus L'académie Sci. Paris* **1971**, *272*, 2052–2055.
7. Festa, V.; Fornelli, A.; Paglionico, A.; Pascazio, A.; Piccarreta, G.; Spiess, R. Asynchronous extension of the late-Hercynian crust in Calabria. *Tectonophysics* **2012**, *518–521*, 29–43. [CrossRef]
8. Del Moro, A.; Fornelli, A.; Piccarreta, G. Tectonothermal history of the Hercynian continental crust of the Serre (Southern Calabria, Italy) monitored by Rb-Sr biotite resetting. *Terra Nova* **2000**, *12*, 239–244. [CrossRef]
9. Bonardi, G.; Cavazza, W.; Perrone, V.; Rossi, S. Calabria-Peloritani terrane and northern Ionian Sea. In *Anatomy of an Orogen: The Apennines and Adjacent Mediterranean Basins*; Springer: Dutch, The Netherlands, 2001; pp. 287–306.
10. Amodio-Morelli, L.; Bonardi, G.; Colonna, V.; Dietrich, D.; Giunta, G.; Ippolito, F.; Liguori, V.; Lorenzoni, S.; Paglionico, A.; Perrone, V.; et al. L'Arco Calabro-Peloritano nell'Orogene Appenninico-Maghrebide. *Mem. Della Soc. Geol. Ital.* **1976**, *17*, 1–60.
11. Cavalcante, F.; Belviso, C.; Laurita, S.; Prosser, G. P-T constraints from phyllosilicates of the Liguride complex of the Pollino area (Southern Apennines, Italy): Geological inferences. *Ofioliti* **2012**, *37*, 65–75. [CrossRef]
12. Liberi, F.; Morten, L.; Piluso, E. Geodynamic significance of ophiolites within the Calabrian Arc. *Isl. Arc* **2006**, *15*, 26–43. [CrossRef]
13. Fedele, L.; Tramparulo, F.D.A.; Vitale, S.; Cappelletti, P.; Prinzi, E.P.; Mazzoli, S. Petrogenesis and deformation history of the lawsonite-bearing blueschist facies metabasalts of the Diamante-Terranova oceanic unit (southern Italy). *J. Metamorph. Geol.* **2018**, *36*, 691–714. [CrossRef]
14. Vitale, S.; Ciarcia, S. Tectono-stratigraphic and kinematic evolution of the southern Apennines/Calabria–Peloritani Terrane system (Italy). *Tectonophysics* **2013**, *583*, 164–182. [CrossRef]
15. Tursi, F.; Bianco, C.; Brogi, A.; Caggianelli, A.; Prosser, G.; Ruggieri, G.; Braschi, E. Cold subduction zone in northern Calabria (Italy) revealed by lawsonite–clinopyroxene blueschists. *J. Metamorph. Geol.* **2020**, *38*, 451–469. [CrossRef]
16. Rossetti, F.; Goffé, B.; Monié, P.; Faccenna, C.; Vignaroli, G. Alpine orogenic P-T-t-deformation history of the Catena Costiera area and surrounding regions (Calabrian Arc, southern Italy): The nappe edifice of north Calabria revised with insights on the Tyrrhenian-Apennine system formation. *Tectonics* **2004**, *23*, 1–26. [CrossRef]

17. Shimabukuro, D.H.; Wakabayashi, J.; Alvarez, W.; Chang, S.-C. Cold and old: The rock record of subduction initiation beneath a continental margin, Calabria, southern Italy. *Lithosphere* **2012**, *4*, 524–532. [CrossRef]
18. Rossetti, F.; Faccenna, C.; Goffé, B.; Monié, P.; Argentieri, A.; Funiciello, R.; Mattei, M. Alpine structural and metamorphic signature of the Sila Piccola Massif nappe stack (Calabria, Italy): Insights for the tectonic evolution of the Calabrian Arc. *Tectonics* **2001**, *20*, 112–133. [CrossRef]
19. Piccarreta, G. Deep-rooted overthrusting and blueschistic metamorphism in compressive continental margins. An example from Calabria (Southern Italy). *Geol. Mag.* **1981**, *118*, 539–544. [CrossRef]
20. Tursi, F.; Acquafredda, P.; Festa, V.; Fornelli, A.; Langone, A.; Micheletti, F.; Spiess, R. What can high-*P* sheared orthogneisses tell us? An example from the Curinga–Girifalco Line (Calabria, southern Italy). *J. Metamorph. Geol.* **2021**, *39*, 919–944. [CrossRef]
21. Ortolano, G.; Visalli, R.; Fazio, E.; Fiannacca, P.; Godard, G.; Pezzino, A.; Punturo, R.; Sacco, V.; Cirrincione, R. Tectono-metamorphic evolution of the Calabria continental lower crust: The case of the Sila Piccola Massif. *Int. J. Earth Sci.* **2020**, *109*, 1295–1319. [CrossRef]
22. Spiegel, C. Mylonitization, dry shearing and the exhumation of the former lower crust: The Curinga-Girifalco Line (Calabria, South Italy). *Neues Jahrb. Fur Geol. Und Palaontol. Abh.* **2003**, *230*, 359–390. [CrossRef]
23. Festa, V.; Prosser, G.; Caggianelli, A.; Grande, A.; Langone, A.; Mele, D. Vorticity analysis of the Palmi shear zone mylonites: New insights for the Alpine tectonic evolution of the Calabria–Peloritani terrane (southern Italy). *Geol. J.* **2016**, *51*, 670–681. [CrossRef]
24. Festa, V.; Cicala, M.; Tursi, F. The Curinga–Girifalco Line in the framework of the tectonic evolution of the remnant Alpine chain in Calabria (southern Italy). *Int. J. Earth Sci.* **2020**, *109*, 2583–2598. [CrossRef]
25. Pezzino, A.; Angi, G.; Fazio, E.; Fiannacca, P.; Lo Giudice, A.; Ortolano, G.; Punturo, R.; Cirrincione, R.; de Vuono, E. Alpine metamorphism in the aspromonte massif: Implications for a new framework for the southern sector of the Calabria-Peloritani Orogen, Italy. *Int. Geol. Rev.* **2008**, *50*, 423–441. [CrossRef]
26. Heymes, T.; Monié, P.; Arnaud, N.; Pêcher, A.; Bouillin, J.P.; Compagnoni, R. Alpine tectonics in the Calabrian–Peloritan belt (southern Italy): New 40Ar/39Ar data in the Aspromonte Massif area. *Lithos* **2010**, *114*, 451–472. [CrossRef]
27. Schenk, V. The exposed crustal cross section of southern Calabria, Italy: Structure and evolution of a segment of Hercynian crust. In *Exposed Cross-Sections of the Continental Crust*; Sallisbury, M.H., Fountain, D.M., Eds.; Kluwer Academic Publishers: Norwell, MA, USA, 1990; pp. 21–42. ISBN 978-94-010-6788-1.
28. Festa, V.; Di Battista, P.; Caggianelli, A.; Liotta, D. Exhumation and tilting of the late Herchynian continental crust in the Serre Massif (Southern Calabria, Italy). *Boll. Della Soc. Geol. Ital.* **2003**, *2*, 79–88.
29. Tursi, F.; Spiess, R.; Festa, V.; Fregola, R.A. Hercynian subduction-related processes within the metamorphic continental crust in Calabria (southern Italy). *J. Metamorph. Geol.* **2020**, *38*, 771–793. [CrossRef]
30. Paglionico, A.; Piccarreta, G. History and petrology of a fragmant of the deep crust in the Serre (Calabria, southern Italy). *N. Jb. Miner. Mh.* **1978**, *9*, 385–396.
31. Colonna, V.; Piccarreta, G. Schema strutturale della Sila Piccola. *Boll. Della Soc. Geol. Ital.* **1975**, *94*, 3–16.
32. Micheletti, F.; Barbey, P.; Fornelli, A.; Piccarreta, G.; Deloule, E. Latest precambrian to early cambrian U–Pb zircon ages of augen gneisses from Calabria (Italy), with inference to the Alboran microplate in the evolution of the peri-Gondwana terranes. *Int. J. Earth Sci.* **2007**, *96*, 843–860. [CrossRef]
33. Micheletti, F.; Fornelli, A.; Piccarreta, G.; Tiepolo, M. U–Pb zircon data of Variscan meta-igneous and igneous acidic rocks from an Alpine shear zone in Calabria (southern Italy). *Int. J. Earth Sci.* **2011**, *100*, 139–155. [CrossRef]
34. Fornelli, A.; Festa, V.; Micheletti, F.; Spiess, R.; Tursi, F. Building an orogen: Review of U-Pb zircon ages from the Calabria–Peloritani terrane to constrain the timing of the southern variscan belt. *Minerals* **2020**, *10*, 944. [CrossRef]
35. Altenberger, U.; Prosser, G.; Grande, A.; Günter, C.; Langone, A. A seismogenic zone in the deep crust indicated by pseudotachylytes and ultramylonites in granulite-facies rocks of Calabria (Southern Italy). *Contrib. Miner. Pet.* **2013**, *166*, 975–994. [CrossRef]
36. Cardozo, N.; Almendinger, R.W. Spherical projections with OSXStereonet. *Comput. Geosci.* **2013**, *51*, 193–205. [CrossRef]
37. Passchier, C.W.; Trouw, R.A.J. *Microtectonics*; Springer: Berlin/Heidelberg, Germany, 2005; Volume 275, ISBN1 3540640037. ISBN2 9783540640035.
38. Whitney, D.L.; Evans, B.W. Abbreviations for names of rock-forming minerals. *Am. Mineral.* **2010**, *95*, 185–187. [CrossRef]
39. Stipp, M.; Stünitz, H.; Heilbronner, R.; Schmid, S.M. Dynamic recrystallization of quartz: Correlation between natural and experimental conditions. *Geol. Soc. Lond. Spec. Publ.* **2002**, *200*, 171–190. [CrossRef]
40. Hawthorne, F.C.; Oberti, R.; Harlow, G.E.; Maresch, W.V.; Martin, R.F.; Schumacher, J.C.; Welch, M.D. Ima report: Nomenclature of the amphibole supergroup. *Am. Mineral.* **2012**, *97*, 2031–2048. [CrossRef]
41. Powell, R.; Holland, T.J.B. A internally consistent thermodynamic dataset with uncertainties and correlation: 3 Application to geobarometry, worked examples and a computer program. *J. Metamorph. Geol.* **1988**, *6*, 173–204. [CrossRef]
42. Powell, R.; Holland, T. Optimal geothermometry and geobarometry. *Am. Mineral.* **1994**, *79*, 120–133.
43. Holland, T.J.B.; Powell, R. An improved and extended internally consistent thermodynamic dataset for phases of petrological interest, involving a new equation of state for solids. *J. Metamorph. Geol.* **2011**, *29*, 333–383. [CrossRef]
44. Powell, R.; Holland, T.J.B. On thermobarometry. *J. Metamorph. Geol.* **2008**, *26*, 155–179. [CrossRef]
45. Holdaway, M.J.; Mukhopadhyay, B.; Dyar, M.D.; Dutrow, B.L.; Rumble, D.; Grambling, J.A. A new perspective on staurolite crystal chemistry: Use of stoichiometric and chemical end-members for a mole fraction model. *Am. Mineral.* **1991**, *76*, 1910–1919.

46. Holland, T.J.B.; Powell, R. An internally consistent thermodynamic data set for phases of petrological interest. *J. Metamorph. Geol.* **1998**, *16*, 309–343. [CrossRef]
47. Tursi, F.; Festa, V.; Fornelli, A.; Micheletti, F.; Spiess, R. Syn-shearing mobility of major elements in ductile shear zones: State of the art for felsic deformed protoliths. *Period. Di Mineral.* **2018**, *87*, 289–308. [CrossRef]
48. Tursi, F. The key role of μH_2O gradients in deciphering microstructures and mineral assemblages of mylonites: Examples from the Calabria polymetamorphic terrane. *Miner. Pet.* **2022**, *116*, 1–14. [CrossRef]
49. Fornelli, A.; Langone, A.; Micheletti, F.; Piccarreta, G. Time and duration of Variscan high-temperature metamorphic processes in the south European Variscides: Constraints from U-Pb chronology and trace element chemistry of zircon. *Miner. Pet.* **2011**, *103*, 101–122. [CrossRef]
50. Fornelli, A.; Pascazio, A.; Piccarreta, G. Diachronic and different metamorphic evolution in the fossil Variscan lower crust of Calabria. *Int. J. Earth Sci.* **2011**, *101*, 1191–1207. [CrossRef]
51. Jenkin, G.R.T. Mode effects on cooling rate estimates from Rb-Sr data. *Geology* **1997**, *25*, 907–910. [CrossRef]
52. Doglioni, C.; Bosellini, A. Eoalpine and mesoalpine tectonics in the Southern Alps. *Geol. Rundsch.* **1987**, *76*, 735–754. [CrossRef]
53. Thöni, M.; Miller, C. Garnet Sm-Nd data from the Saualpe and the Koralpe (Eastern Alps, Austria): Chronological and P-T constraints on the thermal and tectonic history. *J. Metamorph. Geol.* **1996**, *14*, 453–466. [CrossRef]
54. Schenk, V. U-Pb and Rb-Sr radiometric dates and their correlation with metamorphic events in the granulite-facies basement of the Serre, Southern Calabria (Italy). *Contrib. Miner. Pet.* **1980**, *73*, 23–38. [CrossRef]